

# Three-dimensional ferromagnetism and magnetotransport in van der Waals Mn-intercalated tantalum disulfide

Yu Liu,<sup>1,\*</sup> Zhixiang Hu,<sup>1,2</sup> Eli Stavitski,<sup>3</sup> Klaus Attenkofer,<sup>3,†</sup> and C. Petrovic<sup>1,2</sup>

<sup>1</sup>*Condensed Matter Physics and Materials Science Department,  
Brookhaven National Laboratory, Upton, New York 11973, USA*

<sup>2</sup>*Materials Science and Chemical Engineering Department,  
Stony Brook University, Stony Brook, New York 11790, USA*

<sup>3</sup>*National Synchrotron Light Source II, Brookhaven National Laboratory, Upton, New York 11973, USA*

(Dated: January 23, 2022)

Van der Waals (vdW) ferromagnets are an important class of materials for spintronics applications. The recent discovery of atomically vdW magnets CrI<sub>3</sub> and Cr<sub>2</sub>Ge<sub>2</sub>Te<sub>6</sub> has triggered a renaissance in the area of two-dimensional (2D) magnetism. Herein we systematically studied 2H-Mn<sub>0.28</sub>TaS<sub>2</sub> single crystal, a 2D vdW ferromagnet with  $T_c \sim 82.3$  K and a large in-plane magnetic anisotropy. Mn *K*-edge x-ray absorption spectroscopy was measured to provide information on its electronic state and local atomic environment. The detailed magnetic isotherms measured in the vicinity of  $T_c$  indicates that the spin coupling inside 2H-Mn<sub>0.28</sub>TaS<sub>2</sub> is of a three-dimensional (3D) Heisenberg-type coupled with the attractive long-range interaction between spins that decay as  $J(r) \approx r^{-4.85}$ . Both resistivity  $\rho(T)$  and thermopower  $S(T)$  exhibit anomalies near  $T_c$ , confirming that the hole-type transport carriers strongly interact with local moments. An unusual angle-dependent magnetoresistance is further observed, suggesting a possible field-induced novel magnetic structure.

## INTRODUCTION

Layered vdW materials attract great interest due to their remarkable physical properties and applications in electronic/spintronic devices [1–4]. Recently, several notable intrinsic vdW magnets have been observed in mono-/few-layer of FePS<sub>3</sub>, Cr<sub>2</sub>Ge<sub>2</sub>Te<sub>6</sub>, CrI<sub>3</sub>, Fe<sub>3</sub>GeTe<sub>2</sub>, VSe<sub>2</sub>, and MnSe<sub>2</sub>, of high interest in spintronic and in fundamental 2D magnetism alike [5–10].

Magnetic critical behavior gives insight into the nature of magnetic interactions, correlation length, spin dimensionality, and the spatial decay of correlation function at criticality [11, 12]. Three principal spin Hamiltonians are reported in MPS<sub>3</sub> (M = transition metal): 2D Heisenberg type in MnPS<sub>3</sub>, 2D XY type in NiPS<sub>3</sub>, and 2D Ising type in FePS<sub>3</sub> [13]. Moreover, 2D Ising-like critical behavior is observed in bulk Cr<sub>2</sub>Si<sub>2</sub>Te<sub>6</sub> and Cr<sub>2</sub>Ge<sub>2</sub>Te<sub>6</sub> [14–17], however 3D critical exponents are found in bulk Fe<sub>3</sub>GeTe<sub>2</sub>, CrI<sub>3</sub>, and Mn<sub>3</sub>Si<sub>2</sub>Te<sub>6</sub>, as a result of the different strengths of interlayer coupling [18–22]. The magnetic properties can further be tuned by thickness variation, as for example a crossover 3D-2D behavior in thickness-reduced CrI<sub>3</sub> and Fe<sub>3</sub>GeTe<sub>2</sub> [23, 24]. In addition, intercalated transition metal dichalcogenides commonly feature *3d* atoms in the vdW gap and host diverse magnetic orders [25–29]. A notable example is 2H-Fe<sub>0.25</sub>TaS<sub>2</sub>, the only member that exhibit ferromagnetic (FM) order with a strong uniaxial anisotropy, similar to recently investigated 2D vdW magnets. 2H-Fe<sub>0.25</sub>TaS<sub>2</sub> features large magnetocrystalline anisotropy, magnetoresistance (MR), and sharp switching in magnetization [30–32]. 2H-Mn<sub>*x*</sub>TaS<sub>2</sub> has been found to be FM but with an easy-plane anisotropy [33–38].

In this work, we systematically studied the magnetic critical behavior and magnetotransport properties of 2H-Mn<sub>0.28</sub>TaS<sub>2</sub> single crystal, with relatively high  $T_c$  of 82.3 K and large in-plane anisotropy. Critical exponents  $\beta = 0.57(1)$ ,  $\gamma = 1.27(3)$ , and  $\delta = 3.51(1)$  are close to those calculated via renormalization group approach for a 3D Heisenberg model coupled with attractive long-range interaction between spins that decay as  $J(r) \approx r^{-4.85}$ . 2H-Mn<sub>0.28</sub>TaS<sub>2</sub> shows a metallic behavior in resistivity  $\rho(T)$  and positive values of thermopower  $S(T)$  with dominant hole-type carriers, in which obvious anomalies were observed corresponding to the magnetic transition. The observed unusual angle-dependent MR suggests a change of magnetic state in magnetic field.

## EXPERIMENTAL DETAILS

The single crystals were fabricated by chemical vapor transport method with iodine agent. A mixture of Mn, Ta, and S powder with a nominal mole ratio of 0.5 : 1 : 2 was sealed in an evacuated quartz tube and then heated for two weeks in a two-zone furnace with the source zone temperature of 1000 °C and the growth zone temperature of 900 °C, respectively. The obtained single crystals are hexagonal shape with typical dimensions as  $2 \times 2 \times 0.5$  mm<sup>3</sup>. The average stoichiometry was determined by examination of multiple points on fresh surface and checked by multiple samples from the same batch using energy-dispersive x-ray spectroscopy in a JEOL LSM-6500 scanning electron microscope. The actual element ratio is Mn<sub>0.28(1)</sub>TaS<sub>1.88(2)</sub> with Ta fixed to 1.0, which is referred to as Mn<sub>0.28</sub>TaS<sub>2</sub> throughout this paper due to  $\sim 5\%$  sulfur deficiency is normally observed in transition-metal

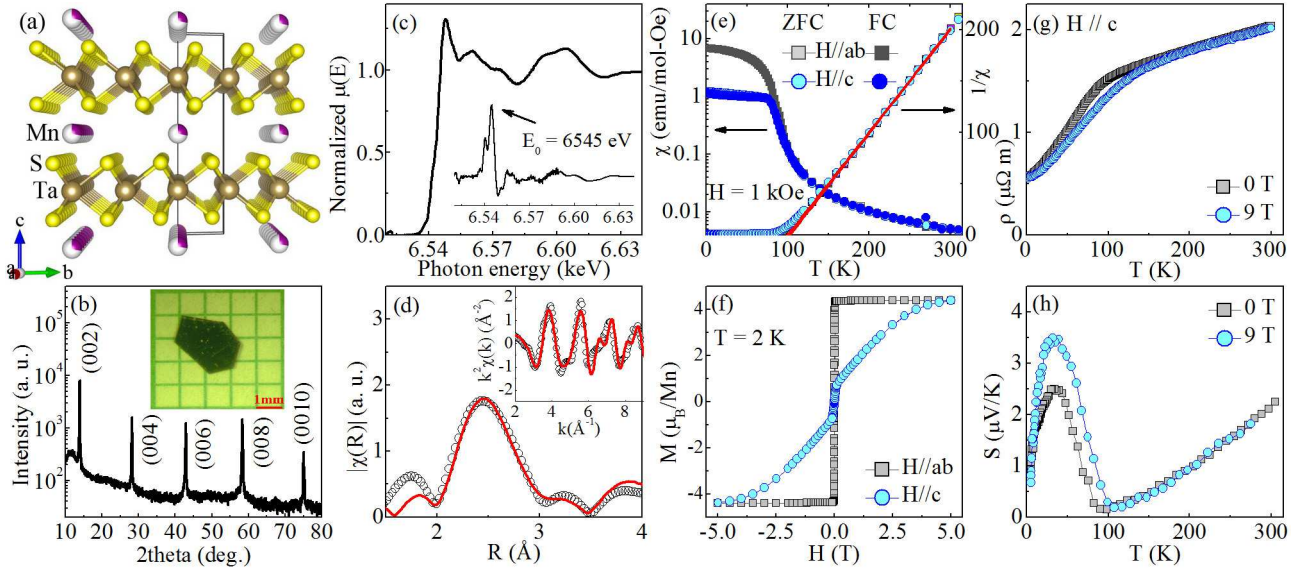


FIG. 1. (Color online) (a) Crystal structure and (b) x-ray diffraction (XRD) pattern in logarithmic scale of  $2\text{H-Mn}_{0.28}\text{TaS}_2$ . Inset in (b) shows the representative single crystal. (c) Normalized Mn  $K$ -edge x-ray absorption near edge structure (XANES) spectra. Inset shows the derivative  $\mu(E)$  curve. (d) Fourier transform magnitudes of the extended x-ray absorption fine structure (EXAFS) oscillations (symbols) for Mn  $K$ -edge with the phase shift correction. The model fits are shown as solid lines. Inset shows the corresponding filtered EXAFS (symbols) with  $k$ -space model fits (solid lines). (e) Temperature-dependent magnetic susceptibility  $\chi(T)$  (left axis) and inverse susceptibility  $1/\chi(T)$  (right axis) with zero-field cooling (ZFC) and field cooling (FC) processes for  $\mathbf{H} \parallel \mathbf{c}$ -axis and  $\mathbf{H} \parallel \mathbf{ab}$ -plane, respectively. The solid straight lines show the Curie-Weiss law fits from 150 to 300 K (right axis). (f) Field-dependent magnetization at 2 K for  $\mathbf{H} \parallel \mathbf{c}$ -axis and  $\mathbf{H} \parallel \mathbf{ab}$ -plane, respectively. Temperature dependence of in-plane (g) resistivity  $\rho(T)$  and (h) thermopower  $S(T)$  in 0 and 9 T.

disulfide. X-ray diffraction (XRD) pattern was acquired on a Rigaku Miniflex powder diffractometer with Cu  $K_\alpha$  ( $\lambda = 0.15418$  nm). X-ray absorption spectroscopy was measured at 8-ID beamline of the National Synchrotron Light Source II (NSLS II) at Brookhaven National Laboratory (BNL) in the fluorescence mode. The x-ray absorption near edge structure (XANES) and extended X-ray absorption fine structure (EXAFS) spectra were processed using the Athena software package. The EXAFS signal,  $\chi(k)$ , was weighed by  $k^2$  to emphasize the high-energy oscillation and then Fourier-transformed in  $k$  range from 2 to  $10 \text{ \AA}^{-1}$  to analyze the data in  $R$  space. The electrical, thermal transport, and magnetization were measured in quantum design PPMS-9 and MPMS-5 instruments.

## RESULTS AND DISCUSSIONS

Figure 1(a,b) exhibits the crystal structure and XRD  $2\theta$  scan in logarithmic scale at room temperature for  $2\text{H-Mn}_{0.28}\text{TaS}_2$  single crystal. The observed sharp peaks can be indexed with (00l) planes, indicating the high quality of crystal and that the plate surface of crystal is normal to the  $\mathbf{c}$ -axis. The lattice parameter  $c = 12.66(2) \text{ \AA}$  can be extracted by using the Bragg's law, close to the value of  $12.62 \text{ \AA}$  in ref.[33]. Figure 1(c) exhibits the nor-

malized Mn  $K$ -edge XANES spectroscopy. The threshold energy  $E_0 = 6545 \text{ eV}$  obtained from the peak of derivative curve [inset in Fig. 2(c)] indicates a mixed 2+ and 3+ valence but close to  $\text{Mn}^{2+}$  state [39]. Figure 1(d) exhibits the Fourier transform magnitudes of EXAFS. In a single-scattering approximation, the EXAFS could be described by [40]:

$$\chi(k) = \sum_i \frac{N_i S_0^2}{k R_i^2} f_i(k, R_i) e^{-\frac{2R_i}{\lambda}} e^{-2k^2 \sigma_i^2} \sin[2kR_i + \delta_i(k)],$$

where  $N_i$  is the number of neighbouring atoms at a distance  $R_i$  from the photoabsorbing atom.  $S_0^2$  is the passive electrons reduction factor,  $f_i(k, R_i)$  is the backscattering amplitude,  $\lambda$  is the photoelectron mean free path,  $\delta_i$  is the phase shift, and  $\sigma_i^2$  is the correlated Debye-Waller factor measuring the mean square relative displacement of the photoabsorber-backscatter pairs. The main peak corresponds well to the six nearest-neighbor Mn-S [ $2.50(1) \text{ \AA}$ ] and then two next-nearest Mn-Ta [ $3.12(11) \text{ \AA}$ ] in the Fourier transform magnitudes of EXAFS [Fig. 1(d)], extracted from the model fit with fixed coordination number and  $\sigma^2 = 0.006 \text{ \AA}^2$ . The peaks above  $3.5 \text{ \AA}$  are due to the longer bond distances and the multiple scattering behavior. Local crystal structure environment of Mn atom shows that Mn is well intercalated in the vdW gap of  $2\text{H-TaS}_2$  crystal.

Figure 1(e) shows the temperature-dependent mag-

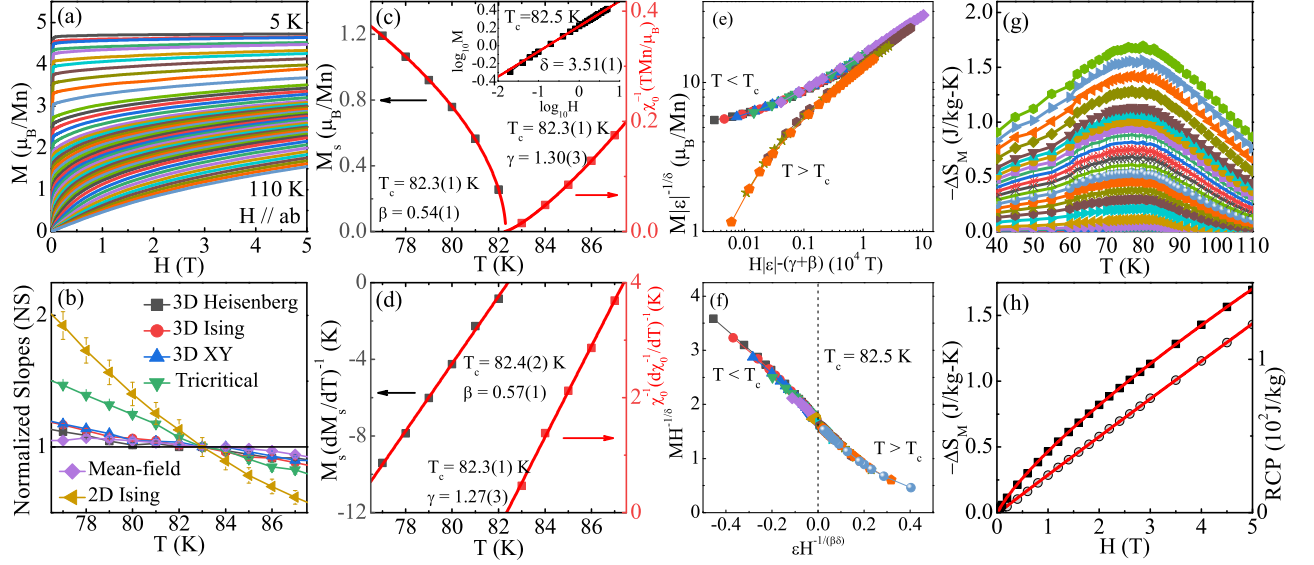


FIG. 2. (Color online) (a) Typical initial isothermal magnetization curves measured with  $\mathbf{H} \parallel \mathbf{ab}$ -plane from 5 to 110 K with temperature steps (5-55 K: 5K; 60-68 K: 2K; 70-89 K: 1 K; 90-110 K: 2K) for  $2\text{H-Mn}_{0.28}\text{TaS}_2$ . (b) Temperature-dependent normalized slopes  $NS = S(T)/S(T_c)$  for different theoretical models. (c) Temperature-dependent spontaneous magnetization  $M_s$  (left axis) and inverse initial susceptibility  $\chi_0^{-1}$  (right axis) with solid fitting curves with  $\mathbf{H} \parallel \mathbf{ab}$ -plane. Inset shows the  $\log_{10}M$  vs  $\log_{10}H$  at 82.5 K with linear fitting curve. (d) Kouvel-Fisher plots of  $M_s(dM_s/dT)^{-1}$  (left axis) and  $\chi_0^{-1}(d\chi_0^{-1}/dT)^{-1}$  (right axis) with solid fitting curves. (e) Scaling plots of  $m$  vs  $h$  with the renormalized magnetization  $m \equiv \varepsilon^{-\beta}M(H, \varepsilon)$  and the renormalized field  $h \equiv \varepsilon^{-(\beta+\gamma)}H$  below and above  $T_c$ , respectively. (f) The rescaling plots of the  $M(H)$  curves by  $MH^{-1/\delta}$  vs  $\varepsilon H^{-1/(\beta\delta)}$ . (g) The calculated magnetic entropy change  $-\Delta S_M^{ax}$  and the relative cooling power RCP with power law fitting in solid lines.

netic susceptibility measured in  $H = 1$  kOe applied in  $\mathbf{ab}$ -plane and along  $\mathbf{c}$ -axis with zero-field cooling (ZFC) and field cooling (FC) processes, respectively. A sharp upturn was observed for both field directions when temperature decreases, suggesting a PM-FM transition. The ZFC and FC data overlap well below  $T_c$ , for both orientations, indicating the high quality of single crystal. The  $\chi(T)$  is nearly isotropic at high temperature, while significant anisotropy is observed at low temperature. The value of  $\chi(T)$  for  $\mathbf{H} \parallel \mathbf{ab}$ -plane is much larger than that for  $\mathbf{H} \parallel \mathbf{c}$ -axis at base temperature, indicating that the magnetic moments of Mn ions tend to be arranged in the  $\mathbf{ab}$  plane. The  $1/\chi(T)$  from 150 to 300 K can be well fitted by the Curie-Weiss law  $\chi = \chi_0 + C/(T - \theta)$  [right axis in Fig. 2(e)], where  $\chi_0$  is a temperature-independent term,  $C$  and  $\theta$  are the Curie-Weiss constant and Weiss temperature, respectively. The obtained Weiss temperature of  $\theta_{ab} = 102(1)$  K and  $\theta_c = 100(1)$  K for  $\mathbf{H} \parallel \mathbf{ab}$ -plane and  $\mathbf{H} \parallel \mathbf{c}$ -axis, respectively, the positive values confirming dominance of FM exchange interactions in  $2\text{H-Mn}_{0.28}\text{TaS}_2$  single crystal. The derived effective moment  $P_{\text{eff}}$  of  $5.40(2)$   $\mu_B/\text{Mn}$  for  $\mathbf{H} \parallel \mathbf{ab}$ -plane and  $5.35(2)$   $\mu_B/\text{Mn}$  for  $\mathbf{H} \parallel \mathbf{c}$ -axis, which are intermediate in value between the spin-only moments of  $4.9$   $\mu_B$  for  $\text{Mn}^{3+}$  and  $5.92$   $\mu_B$  for  $\text{Mn}^{2+}$  [33], in line with the XANES analysis. Then we estimate the Rhodes-Wohlfarth ratio (RWR) for  $2\text{H-Mn}_{0.28}\text{TaS}_2$ , which is defined as  $P_c/P_s$  with  $P_c$  cal-

culated from  $P_c(P_c + 2) = P_{\text{eff}}^2$  and  $P_s \sim 4.38(1)$   $\mu_B$  is the saturation moment [41, 42]. RWR is 1 for a localized system and is larger in an itinerant system. Here we obtain the  $\text{RWR} \approx 1.03(1)$ , indicating a localized character [43]. The mechanism of FM coupling in  $2\text{H-Mn}_{0.28}\text{TaS}_2$  is the Ruderman-Kittel-Kasuya-Yosida (RKKY) interaction in which the local spins of intercalated Mn ions align ferromagnetically through the itinerant Ta 5d electrons [43]. Figure 1(f) presents the field-dependent magnetization at 2 K. When  $\mathbf{H} \parallel \mathbf{ab}$ -plane, the magnetization increases sharply at low field and saturates at a very low field  $\sim 0.2$  T, confirming the easy  $\mathbf{ab}$ -plane. No obvious hysteresis loop (coercive field  $H_c < 10$  Oe) was observed, indicating a soft in-plane FM character.

Figure 1(g,h) exhibits the temperature dependence of in-plane resistivity  $\rho(T)$  and thermopower  $S(T)$  of  $2\text{H-Mn}_{0.28}\text{TaS}_2$  in 0 and 9 T. Above 150 K, the linear temperature dependence of  $\rho(T)$  and  $S(T)$  is due to the dominant electron-phonon scattering, similar to  $2\text{H-Mn}_{0.33}\text{TaS}_2$  [38]. With decreasing temperature, both curves show distinct changes in behavior around  $T_c$ , indicating that there is a considerable interaction between transport carriers and local moments. The positive values of  $S(T)$  indicates that hole-type carriers dominate. As is well known, the thermopower  $S(T)$  depends sensitively on the Fermi surface. The  $S(T)$  gradually deviates from the linear  $T$ -dependence below 150 K, and presents

TABLE I. Comparison of critical exponents of 2H-Mn<sub>0.28</sub>TaS<sub>2</sub> with different theoretical models. MAP, KFP, and CI represent the modified Arrott plot, the Kouvel-Fisher plot, and the critical isotherm, respectively.

	Reference	Technique	$T_{c-}$	$T_{c+}$	$\beta$	$\gamma$	$\delta$
2H-Mn <sub>0.28</sub> TaS <sub>2</sub>	This work	MAP	82.3(1)	82.3(1)	0.54(1)	1.30(3)	3.41(1)
	This work	KFP	82.3(1)	82.4(2)	0.57(1)	1.27(3)	3.23(1)
	This work	CI					3.51(1)
2D Ising	[44]	Theory			0.125	1.75	15.0
Mean field	[45]	Theory			0.5	1.0	3.0
3D Heisenberg	[45]	Theory			0.365	1.386	4.8
3D Ising	[45]	Theory			0.325	1.24	4.82
3D XY	[46]	Theory			0.345	1.316	4.81
Tricritical mean field	[47]	Theory			0.25	1.0	5.0

an obvious upturn near  $T_c$  as well as a broad peak around 35(5) K, as shown in Fig. 1(h), reflecting the reconstruction of Fermi surface passing through the magnetic transition and possible phonon- or magnon-drag effect at low temperature.

To obtain a precise  $T_c$  and the nature of PM-FM transition in 2H-Mn<sub>0.28</sub>TaS<sub>2</sub> single crystal, we measured dense magnetization isotherms with  $\mathbf{H} \parallel \mathbf{ab}$ -plane [Fig. 2(a)]. For a second-order phase transition, the critical behavior can be depicted by a series of interrelated critical exponents. Isotherms can be analyzed with the Arrott-Noakes equation of state [44],

$$(H/M)^{1/\gamma} = a\varepsilon + bM^{1/\beta}, \quad (1)$$

where  $\varepsilon = (T - T_c)/T_c$  is the reduced temperature, and  $a$  and  $b$  are constants. The  $\beta$  and  $\gamma$  are critical exponents that are associated with the spontaneous magnetization  $M_s$  below  $T_c$  and the inverse initial susceptibility  $\chi_0^{-1}$  above  $T_c$ , respectively [45–47]:

$$M_s(T) = M_0(-\varepsilon)^\beta, \varepsilon < 0, T < T_c, \quad (2)$$

$$\chi_0^{-1}(T) = (h_0/m_0)\varepsilon^\gamma, \varepsilon > 0, T > T_c, \quad (3)$$

$$M = DH^{1/\delta}, T = T_c, \quad (4)$$

where  $\delta$  is another critical exponent associated with the  $M(H)$  at  $T_c$ . The  $M_0$ ,  $h_0/m_0$  and  $D$  are the critical amplitudes. In the critical region, right values of  $\beta$ ,  $\gamma$ , and  $\delta$  should generate a set of parallel straight lines of  $M^{1/\beta}$  vs  $(H/M)^{1/\gamma}$  in high field region. The normalized slope  $NS = S(T)/S(T_c)$  with  $S(T) = dM^{1/\beta}/d(H/M)^{1/\gamma}$  enables us to identify the most suitable model by comparing  $NS$  with the ideal value of 1 [Fig. 2(b)]. As we can see, the  $NS$  of mean-field model is mostly close to 1 below  $T_c$ , and it overlaps with 3D Heisenberg and 3D XY models within experimental errors above  $T_c$ , but much better than 2D Ising and tricritical mean-field models, indicating a clear 3D critical behavior in 2H-Mn<sub>0.28</sub>TaS<sub>2</sub>.

Figure 2(c) presents the extracted  $M_s(T)$  and  $\chi_0^{-1}(T)$  as a function of temperature by using a rigorous iterative method [48, 49]. According to Eqs. (2) and (3), the  $\beta = 0.54(1)$ ,  $\gamma = 1.30(3)$ , and  $T_c = 82.3(1)$  K, are derived. The  $\delta$  can be determined directly from the inverse slope of the critical isotherm in log-scale taking into account that  $M = DH^{1/\delta}$ . A linear fit of  $\log_{10}M$  vs  $\log_{10}H$  at  $T_c = 82.5$  K results in  $\delta = 3.51(1)$  [inset in Fig. 2(c)], which is very close to the value of 3.41(1) calculated from the Widom scaling relation  $\delta = 1 + \gamma/\beta$  [50]. In the Kouvel-Fisher relation [51]:

$$M_s(T)[dM_s(T)/dT]^{-1} = (T - T_c)/\beta, \quad (5)$$

$$\chi_0^{-1}(T)[d\chi_0^{-1}(T)/dT]^{-1} = (T - T_c)/\gamma. \quad (6)$$

Linear fittings to the plots of  $M_s(T)[dM_s(T)/dT]^{-1}$  and  $\chi_0^{-1}(T)[d\chi_0^{-1}(T)/dT]^{-1}$  in Fig. 2(d) yield  $\beta = 0.57(1)$  with  $T_c = 82.4(2)$  K, and  $\gamma = 1.27(3)$  with  $T_c = 82.3(1)$  K, in agreement with the values obtained from the modified Arrott plot [Table I]. The  $\beta$  for 2D magnets should be located in a universal window  $\sim 0.1 \leq \beta \leq 0.25$  [52]. That is to say, the critical exponents of 2H-Mn<sub>0.28</sub>TaS<sub>2</sub> exhibit apparent 3D critical phenomenon.

Scaling analysis can be used to estimate the reliability of the obtained  $\beta$ ,  $\gamma$ ,  $\delta$ , and  $T_c$ . The magnetic equation of state in the critical region is expressed as [45]:

$$M(H, \varepsilon) = \varepsilon^\beta f_\pm(H/\varepsilon^{\beta+\gamma}), \quad (7)$$

where  $f_+$  for  $T > T_c$  and  $f_-$  for  $T < T_c$ , respectively, are the regular functions. Eq. (7) can be further written in terms of scaled magnetization  $m \equiv \varepsilon^{-\beta}M(H, \varepsilon)$  and scaled field  $h \equiv \varepsilon^{-(\beta+\gamma)}H$  as  $m = f_\pm(h)$ . This suggests that for true scaling relations and the right choice of  $\beta$ ,  $\gamma$ , and  $\delta$ , scaled  $m$  and  $h$  will fall on universal curves above  $T_c$  and below  $T_c$ , respectively. The scaled  $m$  vs  $h$  curves are plotted in Fig. 2(e). Obviously the lines are separated into two branches below and above  $T_c$ , respectively. This can be further verified by another form of scaling

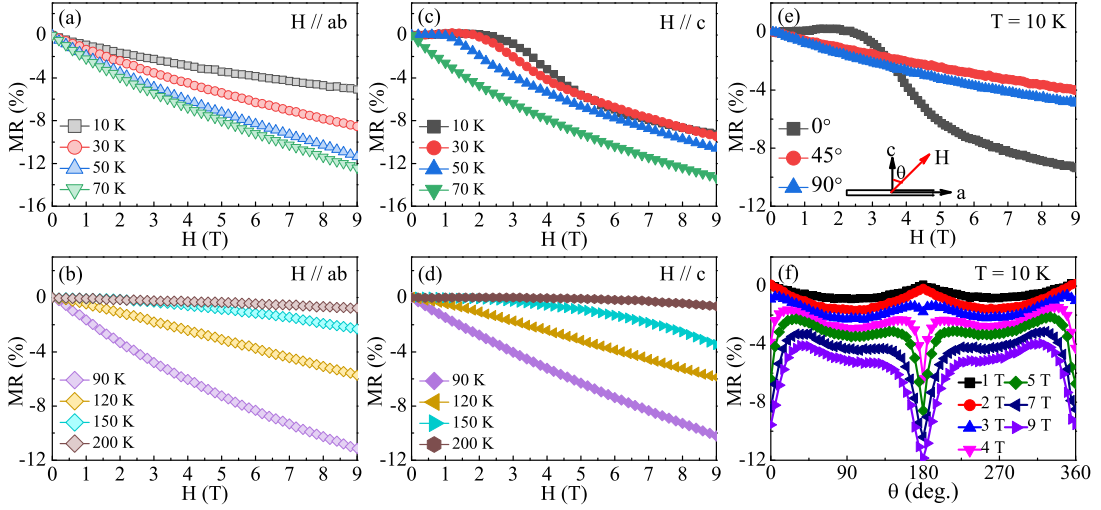


FIG. 3. (Color online) Field-dependent magnetoresistance (MR) with current injected in the **ab**-plane for (a,b)  $\mathbf{H} \parallel \mathbf{ab}$ -plane and (c,d)  $\mathbf{H} \parallel \mathbf{c}$ -axis at various temperatures, respectively. (e,f) Angle-dependent MR measured at  $T = 10$  K for 2H-Mn<sub>0.28</sub>TaS<sub>2</sub>.

equation of state [45],

$$\frac{H}{M^\delta} = k \left( \frac{\varepsilon}{H^{1/\beta}} \right), \quad (8)$$

where  $k(x)$  is the scaling function. According to Eq. (8), the plot of  $MH^{-1/\delta}$  vs  $\varepsilon H^{-1/(\beta\delta)}$  should correspond to one universal curve [53], which is indeed seen in Fig. 2(f), the  $T_c$  locates at the zero point of the horizontal axis. The well-rescaled curves ensure that the obtained critical exponents and  $T_c$  are reliable and intrinsic. Figure 2(g) presents the derived magnetic entropy change  $-\Delta S_M = \int_0^H [\partial M(T, H)/\partial T]_H dH$  (left axis) [54]. It shows a broad peak centered near  $T_c$  and the peak value monotonically increases with increasing field, reaches  $1.70 \text{ J kg}^{-1} \text{ K}^{-1}$  in 5 T. The relative cooling power  $RCP = -\Delta S_M^{max} \times \delta T_{FWHM}$  is also plotted (right axis), where  $-\Delta S_M^{max}$  is the maximum entropy change near  $T_c$  and  $\delta T_{FWHM}$  is the full-width at half maxima [55]. The field dependence of  $-\Delta S_M^{max}$  and  $RCP$  at  $T_c$  shows a power law  $-\Delta S_M^{max} = aH^b$  and  $RCP = cH^d$  [56], where  $c$  and  $d$  are related to the critical exponents as  $b = 1 + (\beta - 1)/(\beta + \gamma)$  and  $d = 1 + 1/\delta$ , respectively. Fitting of  $-\Delta S_M^{max}$  and  $RCP$  gives  $b = 0.79(1)$  and  $d = 1.00(2)$ , which are close to the values of  $b = 0.75(2)$  and  $d = 1.29(1)$  calculated from the obtained  $\beta$ ,  $\gamma$ , and  $\delta$ . This can avoid the multi-step nonlinear fitting induced deviation in the modified Arrott plot and Kouvel-Fisher plot, further verify the reliability and intrinsic of obtained critical exponents.

Then we discuss the nature as well as the range of magnetic interaction in 2H-Mn<sub>0.28</sub>TaS<sub>2</sub>. In renormalization group theory analysis the interaction decays with distance  $r$  as  $J(r) \approx r^{-(3+\sigma)}$ , where  $\sigma$  is a positive constant

[57]. The susceptibility exponent  $\gamma$  is:

$$\gamma = 1 + \frac{4}{d} \left( \frac{n+2}{n+8} \right) \Delta\sigma + \frac{8(n+2)(n-4)}{d^2(n+8)^2} \times \left[ 1 + \frac{2G(\frac{d}{2})(7n+20)}{(n-4)(n+8)} \right] \Delta\sigma^2, \quad (9)$$

where  $\Delta\sigma = (\sigma - \frac{d}{2})$  and  $G(\frac{d}{2}) = 3 - \frac{1}{4}(\frac{d}{2})^2$ ,  $n$  is the spin dimensionality [58]. When  $\sigma > 2$ , the Heisenberg model is valid and  $J(r)$  decreases faster than  $r^{-5}$ . When  $\sigma \leq 3/2$ , the mean-field model is satisfied and  $J(r)$  decreases slower than  $r^{-4.5}$ . Here it is found that  $\{d : n\} = \{3 : 3\}$  and  $\sigma = 1.85$  give the exponents mostly close to the experimental values in 2H-Mn<sub>0.28</sub>TaS<sub>2</sub>. Furthermore, we obtain the correlation length critical exponent  $\nu = 0.697$  ( $\nu = \gamma/\sigma$ ,  $\xi = \xi_0 |(T - T_c)/T_c|^{-\nu}$ ), and  $\alpha = -0.092$  ( $\alpha = 2 - \nu d$ ), also close to the theoretical value (-0.12) for 3D Heisenberg model [59, 60]. Having delineated salient features of magnetic state, we now turn to investigation of electronic transport in magnetic field.

Figure 3(a-d) exhibits the MR measured with  $\mathbf{H} \parallel \mathbf{ab}$ -plane and  $\mathbf{H} \parallel \mathbf{c}$ -axis, respectively, at various temperatures with the current injected in the **ab**-plane. When  $\mathbf{H} \parallel \mathbf{ab}$ -plane, the values of MR are negative in the whole temperature range and reach a maximum  $\sim 12.4\%$  at 70 K, which is normally expected in an in-plane FM thin crystal [61, 62]. It is very interesting that the MR features a plateau or shoulder in low field with positive values at low temperature [Fig. 3(c)]. The maximum  $\sim 13.4\%$  is observed with  $\mathbf{H} \parallel \mathbf{c}$ -axis at 70 K, and the field-dependent MR exhibits a similar tendency compared with those in  $\mathbf{H} \parallel \mathbf{ab}$ -plane when  $T \geq 70$  K. This unusual plateau feature is more apparent at lower temperature, which might be associated with a novel field-induced magnetic structure. A similar behavior was pre-

viously observed in helical magnetic MnSi nanowire due to field-induced conical or skyrmion state [63]. This unusual anisotropic MR is also plotted in Fig. 3(e) with different field orientations. A detailed angle-dependent MR under different fields at 10 K was further measured [Fig. 3(f)]. The angle-dependent MR shows an obvious two-fold symmetry at 1 T and 2 T, however an extra peak shows up when  $\mathbf{H} \parallel \mathbf{c}$ -axis at 3 T, which grows rapidly and takes over the maximum above 4 T. Hence, a field-induced magnetic structure is likely in 2H-Mn<sub>0.28</sub>TaS<sub>2</sub> single crystals which calls further in-depth investigation as well as its thickness-dependent properties.

## CONCLUSIONS

In summary, we systematically studied the mechanism of the PM-FM transition and magnetotransport in 2H-Mn<sub>0.28</sub>TaS<sub>2</sub> single crystals. The spin interaction in 2H-Mn<sub>0.28</sub>TaS<sub>2</sub> is close to a 3D Heisenberg model coupled with attractive long-range exchange interaction decaying with distance as  $J(r) \approx r^{-4.85}$ . A field-induced novel magnetic structure is proposed based on the unusual angle-dependent MR behavior. It is also of high interest to explore the magnetic properties of 2H-Mn<sub>0.28</sub>TaS<sub>2</sub> at the 2D limit down to a monolayer in future studies due to its large magnetic anisotropy. [The exfoliation of thin samples of such intercalated transition metal dichalcogenides can refer to the method in Ref. \[64\].](#)

## ACKNOWLEDGEMENTS

Work at BNL is supported by the Office of Basic Energy Sciences, Materials Sciences and Engineering Division, U.S. Department of Energy (DOE) under Contract No. DE-SC0012704. This research used the 8-ID beamline of the NSLS II, a U.S. DOE Office of Science User Facility operated for the DOE Office of Science by BNL under Contract No. DE-SC0012704.

\*Present address: Los Alamos National Laboratory, MS K764, Los Alamos NM 87545, USA

†Present address: ALBA Synchrotron Light Source, Cerdanyola del Valles, E-08290 Barcelona, Spain.

---

[1] A. K. Geim and I. V. Grigorieva, *Nature* **499**, 419 (2013).  
 [2] S. Z. Butler, S. M. Hollen, L. Cao, Y. Cui, J. A. Gupta, H. R. Gutiérrez, T. F. Heinz, S. S. Hong, J. Huang, A. F. Ismach, E. J. Haplerin, M. Kuno, V. V. Plashnitsa, R. D. Robinson, R. S. Ruoff, S. Salahuddin, J. Shan, L. Shi, M. G. Spencer, M. Terrones, W. Windl, and J. E. Goldberger, *ACS Nano* **7**, 2898 (2013).

[3] G. R. Bhimanapati, Z. Lin, V. Meunier, Y. Jung, J. Cha, S. Das, D. Xiao, Y. Son, M. S. Strano, V. R. Cooper, L. Liang, S. G. Louie, E. Ringe, W. Zhou, S. S. Kim, R. R. Naik, B. G. Sumpter, H. Terrones, F. Xia, Y. Wang, J. Zhu, D. Akinwande, N. Alem, J. A. Schuller, R. E. Schaak, M. Terrones, and J. A. Robinson, *ACS Nano* **9**, 11509 (2015).  
 [4] K. S. Novoselov, A. Mishchenko, A. Carvalho, and A. H. Castro Neto, *Science* **353**, 461 (2016).  
 [5] J. Lee, S. Lee, J. H. Ryoo, S. Kang, T. Y. Kim, P. Kim, C. Park, J. Park, and H. Cheong, *Nano Lett.* **16**, 7433 (2016).  
 [6] B. Huang, G. Clark, E. Navarro-Moratalla, D. R. Klein, R. Cheng, K. L. Seyler, D. Zhong, E. Schmidgall, M. A. McGuire, D. H. Cobden, W. Yao, D. Xiao, P. Jarillo-Herrero, and X. D. Xu, *Nature* **546**, 270 (2017).  
 [7] C. Gong, L. Li, Z. L. Li, H. W. Ji, A. Stern, Y. Xia, T. Cao, W. Bao, C. Z. Wang, Y. Wang, Z. Q. Qiu, R. J. Cava, S. G. Louie, J. Xia, and X. Zhang, *Nature* **546**, 265 (2017).  
 [8] Y. J. Deng, Y. J. Yu, Y. C. Song, J. Z. Zhang, N. Z. Wang, Z. Y. Sun, Y. F. Yi, Y. Z. Wu, S. W. Wu, J. Y. Zhu, J. Wang, X. H. Chen, and Y. B. Zhang, *Nature* **563**, 94 (2018).  
 [9] M. Bonilla, S. Kolekar, Y. Ma, H. C. Diaz, V. Kalappattil, R. Das, T. Eggers, H. R. Gutierrez, M. Phan, and M. Batzill, *Nat. Nanotechnol.* **13** 289 (2018).  
 [10] D. J. O'Hara, T. Zhu, A. H. Trout, A. S. Ahmed, Y. K. Luo, C. H. Lee, M. R. Brenner, S. Rajan, J. A. Gupta, D. W. McComb, and R. K. Kawakami, *Nano Lett.* **18**, 3125 (2018).  
 [11] M. E. Fisher, *Rev. Mod. Phys.* **46**, 597 (1974).  
 [12] H. E. Stanley, *Rev. Mod. Phys.* **71**, S358 (1999).  
 [13] P. A. Joy and S. Vasudevan, *Phys. Rev. B* **46**, 5425 (1992).  
 [14] B. J. Liu, Y. M. Zou, L. Zhang, S. M. Zhou, Z. Wang, W. K. Wang, Z. Qu, and Y. H. Zhang, *Sci. Rep.* **6**, 33873 (2016).  
 [15] Y. Liu and C. Petrovic, *Phys. Rev. B* **96**, 054406 (2017).  
 [16] W. Liu, Y. Dai, Yu-E. Yang, J. Fan, L. Pi, L. Zhang, and Y. Zhang, *Phys. Rev. B* **98**, 214420 (2018).  
 [17] G. T. Lin, H. L. Zhuang, X. Luo, B. J. Liu, F. C. Chen, J. Yan, Y. Sun, J. Zhou, W. J. Lu, P. Tong, Z. G. Sheng, Z. Qu, W. H. Song, X. B. Zhu, and Y. P. Sun, *Phys. Rev. B* **95**, 245212 (2017).  
 [18] Y. Liu, V. N. Ivanovski, and C. Petrovic, *Phys. Rev. B* **96**, 144429 (2017).  
 [19] B. J. Liu, Y. Zou, S. Zhou, L. Zhang, Z. Wang, H. Li, Z. Qu, and Y. H. Zhang, *Sci. Rep.* **7**, 6184 (2017).  
 [20] G. T. Lin, X. Luo, F. C. Chen, J. Yan, J. J. Gao, Y. Sun, W. Tong, P. Tong, W. J. Lu, Z. G. Sheng, W. H. Song, X. B. Zhu, and Y. P. Sun, *Appl. Phys. Lett.* **112**, 072405 (2018).  
 [21] Y. Liu and C. Petrovic, *Phys. Rev. B* **97**, 014420 (2018).  
 [22] Y. Liu and C. Petrovic, *Phys. Rev. B* **98**, 064423 (2018).  
 [23] Y. Liu, L. J. Wu, X. Tong, J. Li, J. Tao, Y. M. Zhu, and C. Petrovic, *Sci. Rep.* **9**, 13599 (2019).  
 [24] Z. Fei, B. Huang, P. Malinowski, W. Wang, T. Song, J. Sanchez, W. Yao, D. Xiao, X. Zhu, A. F. May, W. Wu, D. H. Cobden, J. Chu, and X. Xu, *Nat. Mater.* **17**, 778 (2018).  
 [25] S. S. P. Parkin and R. H. Friend, *Philos. Mag. B* **41**, 65 (1980).  
 [26] R. H. Friend and A. D. Yoffe, *Advances in Phys.* **36**, 1

- (1987).
- [27] H. Guo, N. Lu, L. Wang, X. Wu, and X. C. Zeng, *J. Phys. Chem. C* **118**, 7242 (2014).
- [28] R. H. Friend, A. R. Beal, and A. D. Yoffe, *Philos. Mag.* **35**, 1269 (1977).
- [29] C. Zhang, Y. Yuan, M. Wang, P. Li, J. Zhang, Y. Wen, S. Zhou, and X. X. Zhang, *Phys. Rev. Mater.* **3**, 114403 (2019).
- [30] E. Morosan, H. W. Zandbergen, L. Li, M. Lee, J. G. Checkelsky, M. Heinrich, T. Siegrist, N. P. Ong, and R. J. Cava, *Phys. Rev. B* **75**, 104401 (2007).
- [31] W. J. Hardy, C.-W. Chen, A. Marcinkova, H. Ji, J. Sinova, D. Natelson, and E. Morosan, *Phys. Rev. B* **91**, 054426 (2015).
- [32] C.-W. Chen, S. Chikara, V. S. Zapf, and E. Morosan, *Phys. Rev. B* **94**, 054406 (2016).
- [33] H. Hinode, T. Ohtani, and M. Wakihara, *J. Solid State Chem.* **114**, 1 (1995).
- [34] Y. Onuki, K. Ina, T. Hirai, and T. Komatsubara, *J. Phys. Soc. Jpn.* **55**, 347 (1986).
- [35] L. D. Cussen, E. A. Marseglia, D. M. Paul, and B. D. Rainford, *Physica B: Condens. Matter* **156-157**, 712 (1989).
- [36] L. J. Li, W. J. Lu, X. D. Zhu, Z. R. Zhang, W. H. Song, and Y. P. Sun, *J. Magn. Magn. Mater.* **323**, 2536 (2011).
- [37] P. M. Shand, C. Cooling, C. Mellinger, J. J. Danker, T. E. Kidd, K. R. Boyle, and L. H. Strauss, *J. Magn. Magn. Mater.* **382**, 49 (2015).
- [38] H. Zhang, W. Wei, G. Zheng, J. Lu, M. Wu, X. Zhu, J. Tang, W. Ning, Y. Han, L. Lin, J. Yang, W. Gao, Y. Qin, and M. Tian, *Appl. Phys. Lett.* **113**, 072402 (2018).
- [39] G. Subías, J. García, M. G. Proietti, and J. Blasco, *Phys. Rev. B* **56**, 8183 (1997).
- [40] R. Prins and D. C. Koningsberger (eds.), *X-ray Absorption: Principles, Applications, Techniques of EXAFS, SEXAFS, XANES* (Wiley, New York, 1988).
- [41] E. P. Wohlfarth, *J. Magn. Magn. Mater.* **7**, 113 (1978).
- [42] T. Moriya, *J. Magn. Magn. Mater.* **14**, 1 (1979).
- [43] K. Motizuki, N. Suzuki, and S. Tomishima, *J. Magn. Magn. Mater.* **104**, 681 (1992).
- [44] A. Arrott, and J. Noakes, *Phys. Rev. Lett.* **19**, 786 (1967).
- [45] H. E. Stanley, *Introduction to Phase Transitions and Critical Phenomena* (Oxford University Press, London and New York, 1971).
- [46] M. E. Fisher, *Rep. Prog. Phys.* **30**, 615 (1967).
- [47] J. Lin, P. Tong, D. Cui, C. Yang, J. Yang, S. Lin, B. Wang, W. Tong, L. Zhang, Y. Zou, and Y. Sun, *Sci. Rep.* **5**, 7933 (2015).
- [48] W. Kellner, M. Fähnle, H. Kronmüller, and S. N. Kaul, *Phys. Status Solidi B* **144**, 387 (1987).
- [49] A. K. Pramanik, and A. Banerjee, *Phys. Rev. B* **79**, 214426 (2009).
- [50] B. Widom, *J. Chem. Phys.* **41**, 1633 (1964).
- [51] J. S. Kouvel, and M. E. Fisher, *Phys. Rev.* **136**, A1626 (1964).
- [52] A. Taroni, S. T. Bramwell, and P. C. W. Holdsworth, *J. Phys.: Condens. Matter*, **20**, 275233 (2008).
- [53] M. Phan, V. Franco, N. Bingham, H. Srikanth, N. Hur, and S. Yu, *J. Alloy. Compd.* **508**, 238 (2010).
- [54] J. Amaral, M. Reis, V. Amaral, T. Mendonc, J. Araujo, M. Sa, P. Tavares, J. Vieira, *J. Magn. Magn. Mater.* **290**, 686 (2005).
- [55] K. A. Gschneidner Jr., V. K. Pecharsky, A. O. Pecharsky, and C. B. Zimm, *Mater. Sci. Forum* **315-317**, 69 (1999).
- [56] V. Franco, J. S. Blazquez, and A. Conde, *Appl. Phys. Lett.* **89**, 222512 (1984).
- [57] M. E. Fisher, S. K. Ma, and B. G. Nickel, *Phys. Rev. Lett.* **29** 917 (1972).
- [58] S. F. Fischer, S. N. Kaul, and H. Kronmuller, *Phys. Rev. B* **65**, 064443 (2002).
- [59] J. C. LeGuillou and J. Zinn-Justin, *Phys. Rev. B* **21**, 3976 (1980).
- [60] M. E. Fisher, *Rev. Mod. Phys.*, **46**, 597 (1974).
- [61] Y. Liu, J. Yang, W. Chu, H. Du, W. Ning, L. Ling, W. Tong, Z. Qu, G. Cao, Y. Zhang, and M. Tian, *Appl. Phys. Lett.* **111**, 033103 (2017).
- [62] Y. Liu, J. Yang, W. Wang, H. Du, W. Ning, L. Ling, W. Tong, Z. Qu, G. Cao, Y. Zhang, and M. Tian, *Phys. Rev. B* **95**, 161103(R) (2017).
- [63] H. F. Du, J. P. DeGrave, F. Xue, D. Liang, W. Ning, J. Y. Yang, M. Tian, Y. Zhang, and S. Jin, *Nano Lett.* **14**, 2026 (2014).
- [64] T. Danz, Q. Liu, X. D. Zhu, L. H. Wang, S. W. Cheong, I. Radu, C. Ropers, and R. I. Tobey, *J. Phys.: Condens. Matter*, **28**, 356002 (2016).